Quasi-Homogeneous Photocatalysis in Ultrastiff Microporous Polymer Aerogels

Yan Su, Bo Li, Zaoming Wang, Alexandre Legrand, Takuma Aoyama, Shuai Fu, Yishi Wu, Ken-Ichi Otake, Mischa Bonn, Hai Wang, et al.

Quasi-Homogeneous Photocatalysis in Ultrastiff Microporous Polymer Aerogels

Yan Su,[‡,§,#] Bo Li,[†,¶,#] Zaoming Wang,[§,#] Alexandre Legrand,[§,¤] Takuma Aoyama,[⊥] Shuai Fu,[∥] Yishi Wu,[|||] Ken-ichi Otake,[§] Mischa Bonn,[∥] Hai I. Wang,[∥,◊] Qing Liao,[|||] Kenji Urayama,[¦] Susumu Kitagawa,[§] Liangbin Huang,[¶,*] Shuhei Furukawa,[§,*] and Cheng Gu[†,*]

[†]College of Polymer Science and Engineering, State Key Laboratory of Polymer Materials Engineering, Sichuan University, Chengdu 610065, P. R. China

[‡]State Key Laboratory of Luminescent Materials and Devices, Institute of Polymer Optoelectronic Materials and Devices, South China University of Technology, No. 381 Wushan Road, Tianhe District, Guangzhou 510640, P. R. China

[§]Institute for Integrated Cell-Material Sciences, Kyoto University, Yoshida, Sakyo-ku, Kyoto 606-8501, Japan

[¶]Key Laboratory of Functional Molecular Engineering of Guangdong Province, School of Chemistry and Chemical Engineering, South China University of Technology, Guangzhou 510641, P. R. China

[⊥]Department of Macromolecular Science and Engineering, Kyoto Institute of Technology, Matsugasaki, Sakyo-ku, Kyoto 606-8585, Japan

[∥]Max Planck Institute for Polymer Research, Ackermannweg 10, 55122 Mainz, Germany

[|||]Beijing Key Laboratory for Optical Materials and Photonic Devices, Department of Chemistry, Capital Normal University, Beijing 100048, P. R. China

[◊]Nanophotonics, Debye Institute for Nanomaterials Science, Utrecht University, Princetonplein 1, 3584 CC Utrecht, The Netherlands

[¤]Unité de Catalyse et Chimie du Solide (UCCS), Université de Lille, CNRS, Centrale Lille, Université d'Artois, UMR 8181, F-59000 Lille, France

[¦]Department of Material Chemistry, Kyoto University, Katsura, Nishikyo-ku, Kyoto 615-8510, Japan

KEYWORDS: conjugated microporous polymers, gels, mechanical strength, quasi-homogeneous photocatalysis, organic transformation

ABSTRACT: The development of efficient and low-cost catalysts is essential for photocatalysis; however, the intrinsically low photocatalytic efficiency, as well as the difficulty in using and recycling photocatalysts in powder morphology, greatly limits their practical performance. Herein, we describe quasi-homogeneous photocatalysis to overcome these two limitations by constructing ultrastiff, hierarchically porous, and photoactive aerogels of conjugated microporous polymers (CMPs). The CMP aerogels exhibit low density but high stiffness beyond 10^5 m^2 s^{-2}, outperforming most low-density materials. Extraordinary stiffness ensures their use as robust scaffolds for scaled photocatalysis and recycling without being damaged at the macroscopic level. A challenging but desirable reaction for direct deaminative borylation is demonstrated using the CMP aerogel-based quasi-homogeneous photocatalysis with gram-scale productivity and record-high efficiency under ambient conditions. Combined terahertz and transient absorption spectroscopic studies unveil the generation of high-mobility free carriers and long-lived excitonic species in the CMP aerogels, underlying the observed superior catalytic performance.

Introduction.

Photocatalysis potentially offers the industry a clean and sustainable method of producing chemicals because of its mild operating conditions and low energy consumption.[1−5] The key to achieving efficient photocatalysis is the rational design of the photocatalysts with suitable band structures and outstanding charge-transport properties to utilize photogenerated electrons and holes fully.[6] Among the great number of semiconducting photocatalysts, conjugated microporous polymers (CMPs) that inherently combine conjugated skeletons with permanent nanopores have aroused intensive research interest.[7] Their tailor-made chemical structures allow for the control of optical properties, while the intrinsically porous structure of CMPs not only guarantees their complete exposure to reagents but also offers confined nanospace for photocatalytic reactions.[8] These features have led to the rapid development of CMP-based photocatalysts applied in various reactions, including water splitting,[9] organic transformation,[10] and polymerization.[11] However, like most

heterogeneous photocatalysis, improving the photocatalytic efficiency of CMPs and shaping the powdery CMPs for practical and recycling use are two major issues that restrict their performance.

According to the basic mechanism of photocatalysis, the essential steps involve the photogeneration of excitons, their dissociation into electrons and holes, and subsequent transport to the catalytic centers.[12] The photogenerated excitons in most CMPs are Frenkel exciton,[13] which are essentially tightly bound electron-hole pairs with large binding energies up to 1 eV, featured by small exciton radii confined within the polymer skeletons. These characteristics largely restrict the separation and transport of charge carriers over CMPs and thus inhibit their overall photocatalytic efficiency. Another critical issue is that CMPs are usually synthesized as insoluble and unprocessable powders.[14] This insoluble nature not only results in resistance at the CMP/reactant/solvent interfaces, restricting the migration/percolation of charge carriers and ionic species between reactants and photocatalysts[15] but also leads to recycling issues, inevitably increasing the cost of photocatalysts. Shaping CMPs into macroscopic objects, such as membranes,[16] foams,[17] and aerogels,[18] is thought to be a possible solution but remains a substantial challenge. Among these macroscopic forms, CMP aerogels are particularly interesting because they combine hierarchical pores at different length scales to provide sufficient space for quasi-homogenous photocatalysis with enhanced transportation of the adsorbed molecules. However, controlled synthesis of CMP aerogels is difficult because the fast polymerization of the CMP monomers normally leads to substantial colloidal particles that uncontrollably aggregate to form precipitated powder products. Even though some CMP aerogels have been reported,[18–20] their mechanical strengths are usually insufficient for scaled photocatalysis and recycling without being macroscopically damaged. Except for the mechanical stability, the wettability of aerogels when applied in the reaction solution is also important for their use as photocatalysts,[21,22] requiring judicious design in the synthesis of CMP aerogels.

Herein, we report the construction of ultrastiff CMP aerogel and its use as a reactor for efficient quasi-homogeneous photocatalysis (Figure 1). The essence of our strategy is to encode a photoactive moiety that can generate long-lived excitonic species into the CMP skeleton and control the gelation process. Specifically, 1,4-diacetylpiperazine-2,5-dione (DAPAO) is used as the N-type building block because it allows the generation of long-lived triplet states in the derived polymers.[23] DAPAO can react with two aldehyde-containing building blocks to afford two CMP gels in near-unity yields in polar solvents such as *N*,*N*-dimethyl formamide (DMF). The gel properties including porosity and mechanical strength are systematically controlled by altering the aldehyde building blocks and the building-block concentrations. The corresponding CMP aerogels, synthesized after solvent exchange and supercritical CO_2 ($scCO_2$) drying of the CMP gels, exhibit low density but high mechanical stiffness, outperforming most inorganic, organic, and hybrid aerogels reported to date. Subsequently, we show the ultrastiff CMP aerogel-based quasi-homogeneous photocatalysis to target the efficient synthesis of arylboronic acids and arylboronates, which are widely used as precursors in transition-metal-catalyzed cross-coupling reactions to construct the basic structures of many functional molecules, such as pharmaceuticals, agricultural chemicals, bioactive natural products, and semiconducting materials.[24] In contrast to the traditional approaches that require rigorous anhydrous conditions, direct deaminative borylation is achieved by our CMP aerogel-based quasi-homogeneous photocatalysis with record-high efficiency, gram-scale productivity, and cycling performance. Spectroscopic study reveals that the CMP aerogels feature attractive charge-transport properties in terms of sub-picosecond ultrafast generation of free carriers with high local mobility and long-lived excitonic species, which endow the CMP aerogels with distinct photocatalytic activity.

Results and Discussion.

Gel synthesis and general characterization.

We employed tetraphenylethene (TPE)- and benzene (Bz)-based building blocks bearing four and three aldehyde groups, respectively, which are linked with DAPAO through Knoevenagel condensation reaction to ensure the formation of three-dimensional (3D) conjugated networks (Figures S1–S3). Subsequently, the CMP gels were synthesized by condensation of TPE or Bz building block with DAPAO at a molar ratio of 1:2 or 2:3 in *N*,*N*-dimethyl formamide (DMF) with triethylamine (TEA) as a catalyst (Figure 1, left panel). The gelation process was confirmed by the time-resolved dynamic light scattering (TR-DLS) measurements (Figures S4–S14). At 80 °C, the reactions of 0.40 M DAPAO with either TPE- or Bz-based building block gave the gelation time of ~320 or ~85 min, respectively (Figures S4, S11). In both cases, the CMP gels were synthesized from different building blocks at various concentrations (0.10, 0.20, 0.30, 0.40, 0.50, and 0.60 M DAPAO, referred to as #1 to #6); increasing the concentration of building blocks resulted in faster gelation time (Figures S7, S14). By performing the gelation in the reaction vessels for 1 day, two monolithic, semitransparent, and self-standing CMP gels were obtained for TPE- and Bz-based systems with orange-red and yellow colors, termed **TPE-PAO-G** and **Bz-PAO-G**, respectively (Figure 1, right panel, Figure S15). After solvent exchange and $scCO_2$ drying, the CMP gels were converted to their corresponding aerogels (termed **TPE-PAO-AG** and **Bz-PAO-AG**, respectively), which retained their macroscopic shapes without collapse or crack (Figure 1, right panel). Moreover, by altering the reaction vessels, the gels and aerogels were synthesized into various shapes, such as chunks and membranes. This processability facilitated the precise measurement of their mechanical and optical properties and allowed them to be adapted to diverse application scenarios. Fourier-transform infrared (FT-IR) spectroscopy and solid-state ^{13}C nuclear magnetic resonance (NMR) experiments revealed the near-unity yield of the reaction (Figures S16–S21). For comparison, we synthesized the corresponding CMP powders (termed **TPE-PAO-P** and **Bz-PAO-P**, respectively) by stirring the 0.10 M DAPAO-containing reaction solution (#1). The powders possessed the same chemical structures as the aerogels (Figures S22, S23) but different macroscopic shapes.

Scanning electron microscopy (SEM) images revealed that the CMP aerogels possessed hierarchically porous networks formed by interconnected colloidal particles with sizes proportional to the building block concentration (Figures S24–S27). Powder X-ray diffraction (PXRD) experiments indicated that the CMP aerogels were amorphous (Figures S28, S29). The thermogravimetric (TG) analysis revealed that **TPE-PAO-AG** and **Bz-PAO-AG** were thermally stable until 260 and 160 °C, respectively (Figures S30,

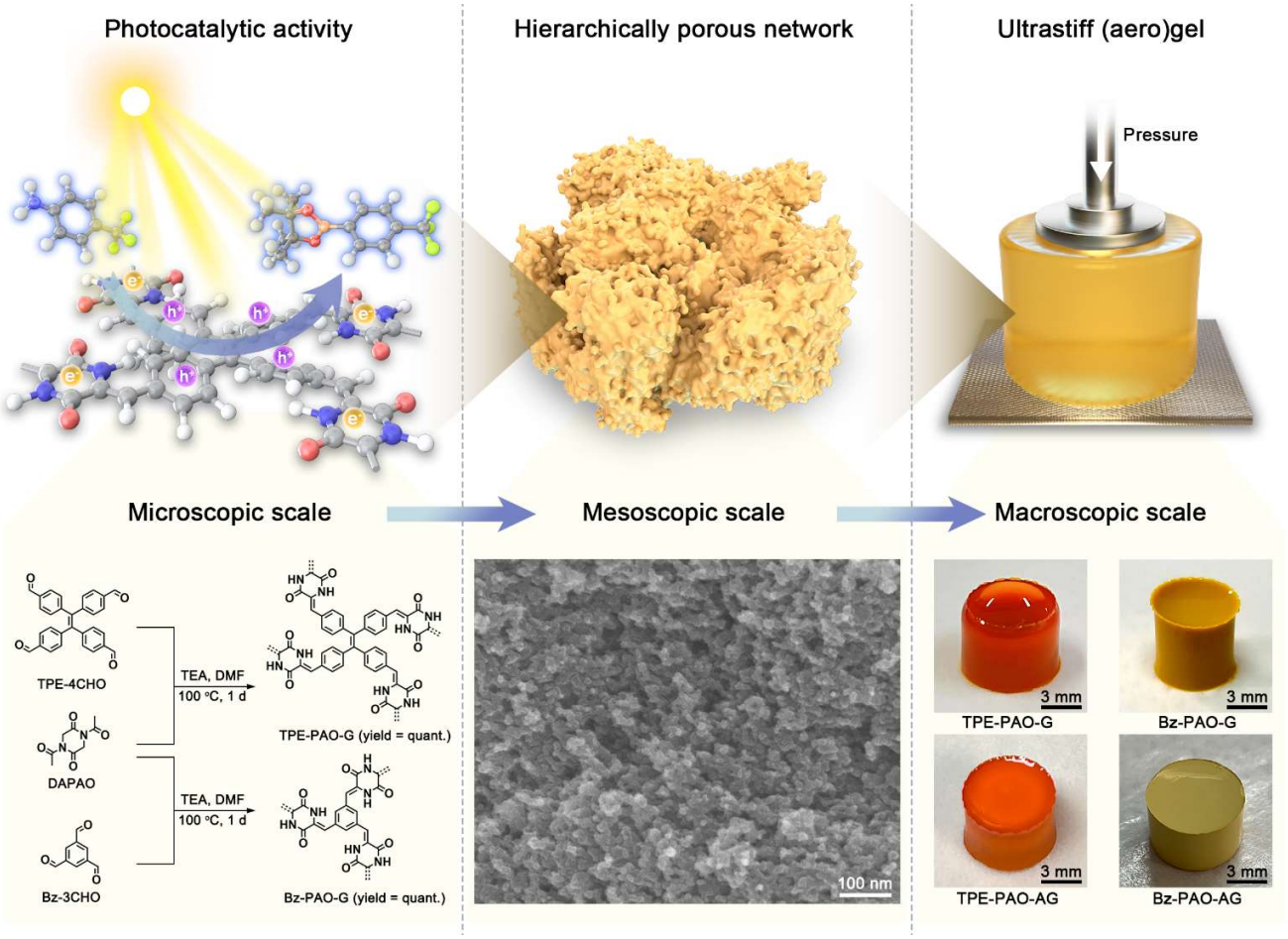

Figure 1. Multiscale depiction of ultrastiff CMP (aero)gel-based quasi-homogeneous photocatalysis. Schematics of the ultrastiff CMP (aero)gels featuring hierarchical colloidal networks constructed from photoactive scaffolds. The left panels show the synthetic routes of **TPE-PAO-G** and **Bz-PAO-G**, with photoactivity of the (aero)gels at the molecular (microscopic) scale. The middle panels depict the hierarchically porous network structure of the colloidal networks at the mesoscopic scale along with the SEM image of **TPE-PAO-AG** (#3). The right panels show the diagrammatic drawing of the stiffness of the (aero)gels (top) and photos of the macroscopic gels and aerogels under natural light (bottom).

S31). We then activated the aerogel samples at 120 °C and measured their nitrogen sorption isotherms at 77 K to evaluate their porosity. Both **TPE-PAO-AG** (#3) and **Bz-PAO-AG** (#4) showed a steep uptake at $P/P_0 < 0.02$ and a slight increase at $0.02 < P/P_0 < 0.8$ (Figures S32, S33), indicative of the micropores and mesopores in the CMP aerogels. At the high-pressure range of $0.8 < P/P_0 < 1$, the CMP aerogels exhibited substantial capillary condensation, evidencing macropores in **TPE-PAO-AG** (#3) and **Bz-PAO-AG** (#4). The hierarchical porosity of the CMP aerogels was also revealed by the pore-size distribution profiles ranging from 0.4 to 50 nm (Figures S34, S35). The nitrogen sorption isotherms of both **TPE-PAO-AG** and **Bz-PAO-AG** indicated that their porosity depends on the building-block concentration: the adsorption capacity initially increased with increasing building-block concentration to subsequently drop beyond a certain threshold concentration (Figures S32, S33). The Brunauer–Emmett–Teller (BET) surface areas and pore volumes of the CMP aerogels revealed volcano-shape profiles with the maximum BET surface areas of 461 and 217 $m^2 g^{-1}$ and the maximum pore volumes of 0.68 and 0.65 $cm^3 g^{-1}$ for **TPE-PAO-AG** (#3) and **Bz-PAO-AG** (#4), respectively (Figures S36–S41). This porosity change could be attributed to a more interconnected colloidal network with more building blocks at higher concentrations, forming more colloidal particles and a denser cross-linked gel network.

Mechanical properties.

The CMP aerogels exhibited low densities (ρ) in the range of 0.019~0.057 and 0.021~0.085 g cm^{-3} for **TPE-PAO-AG** and **Bz-PAO-AG**, respectively (Figure 2a). Indeed, they were so lightweighted that dandelion hairs could even support a relatively large chunk (ca. 160 mg) of the CMP aerogels (Figure 2b, Figure S42). Rheological measurements showed the concentration-dependent mechanical property under the compression mode (Figure 2c, Figures S43, S44). At the low building-block concentration of 0.10 M, both **TPE-PAO-G** and **Bz-PAO-G** showed elasticity with about 50% ultimate compression strain. With increasing the building block concentration, both gels became tougher with substantially enhanced compression strength and decreased elongation at break. This concentration dependency on gel stiffness was further

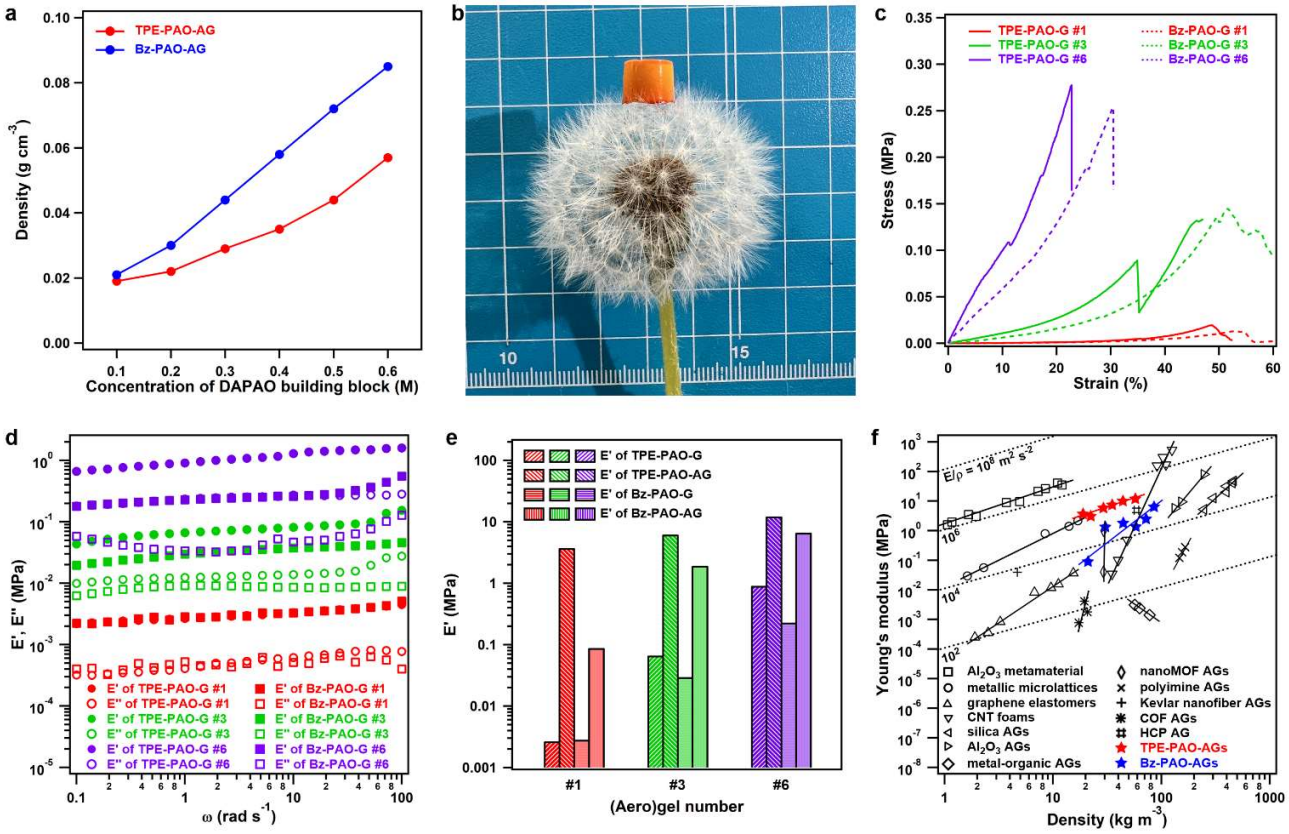

Figure 2. Mechanical properties of the CMP gels and aerogels. (a) The correlation between DAPAO building-block concentration and the density of the CMP aerogels. (b) Photo of a chunk of 160-mg **TPE-PAO-AG** (#3) resting on top of dandelion hairs. (c) Compressive strain-stress curves of **TPE-PAO-G** and **Bz-PAO-G** with different building-block concentrations. (d) Storage Young's modulus (E') (filled circles) and loss Young's modulus (E'') (hollow circles) versus scanning frequency of **TPE-PAO-G** and **Bz-PAO-G** with different building-block concentrations. (e) Summary of storage Young's modulus (E') of **TPE-PAO-G**, **Bz-PAO-G**, **TPE-PAO-AG**, and **Bz-PAO-AG** with different building-block concentrations. (f) An Ashby chart plotting compressive stiffness versus density for ultrastiff CMP aerogels and other previously reported materials. Dotted lines indicate contours of constant stiffness-density ratio $c = E/\rho$ ($m^2 s^{-2}$). Solid lines denote the same family of materials.

supported by the dynamic mechanical analysis (DMA), in which the compression strain was fixed in the elastic region of the gels. All the samples showed characteristic gel-like behavior with frequency-independent storage Young's modulus (E'), which was an order of magnitude higher than their corresponding loss Young's modulus (E''). Compared to **TPE-PAO-G** (#1) and **Bz-PAO-G** (#1) with E' = 2.7×10^{-3} and 2.9×10^{-3} MPa, **TPE-PAO-G** (#6) and **Bz-PAO-G** (#6) presented substantially higher stiffness with E' = 0.91 and 0.23 MPa, respectively (Figure 2d, Figures S45, S46).

Note that the CMP aerogels exhibited enhanced stiffness with the maximum E' values of 12.3 and 6.6 MPa for **TPE-PAO-AG** (#6) and **Bz-PAO-AG** (#6), respectively (Figure 2e, Figures S47, S48), which was 13- and 29-folds of those of gel counterparts, **TPE-PAO-G** (#6) and **Bz-PAO-G** (#6), respectively. The specific stiffness (E'/ρ) of **TPE-PAO-AG** increased linearly with density and was higher than 10^5 m^2 s^{-2}. To the best of our knowledge, this high stiffness outperformed that of most low-density materials, including elastomers,[25] foams,[25] and aerogels made from inorganic carbon/silica/alumina,[26] hybrid metal-organic materials,[27,28] organic linear polymers,[29,30] and crosslinked porous polymers[22, 31] (Figure 2f). The ultrastiffness of **TPE-PAO-AG** is critical for catalytic applications because it ensures their use as robust scaffolds during catalysis without being damaged at the macroscopic level, thus facilitating their practical catalytic handling and recycling performance and eventually decreasing the cost of the catalysts. Moreover, such robust aerogels can withstand certain pressures without being damaged or cracked, thus in principle, they are adaptable to act as matrices for future flow catalysis.[32]

Quasi-homogeneous photocatalysis of deaminative borylation.

To assess the photocatalytic performance of the CMP aerogels, their basic optical properties were characterized. The optical bandgaps of **TPE-PAO-AG** and **Bz-PAO-AG** were estimated to be 2.41 and 2.62 eV, respectively, as evaluated by the UV-vis diffuse reflectance spectra (Figure S49). The highest occupied molecular orbital (HOMO) energy levels measured by ultraviolet photoelectron spectroscopy (UPS) were estimated to be -6.49 and -6.31 eV for **TPE-PAO-AG** and **Bz-PAO-AG**, respectively. The corresponding lowest unoccupied molecular orbital (LUMO) energy levels were calculated to be -4.08 and -3.69 eV (Figures S50, S51). The CMP aerogels exhibited photoluminescence properties with peaks at 575 and 512 nm, quantum yields of 2.5% and 0.1%, and lifetimes of 2.51 and 0.84 ns for **TPE-PAO-AG** and **Bz-PAO-AG**, respectively (Figures S52, S53).

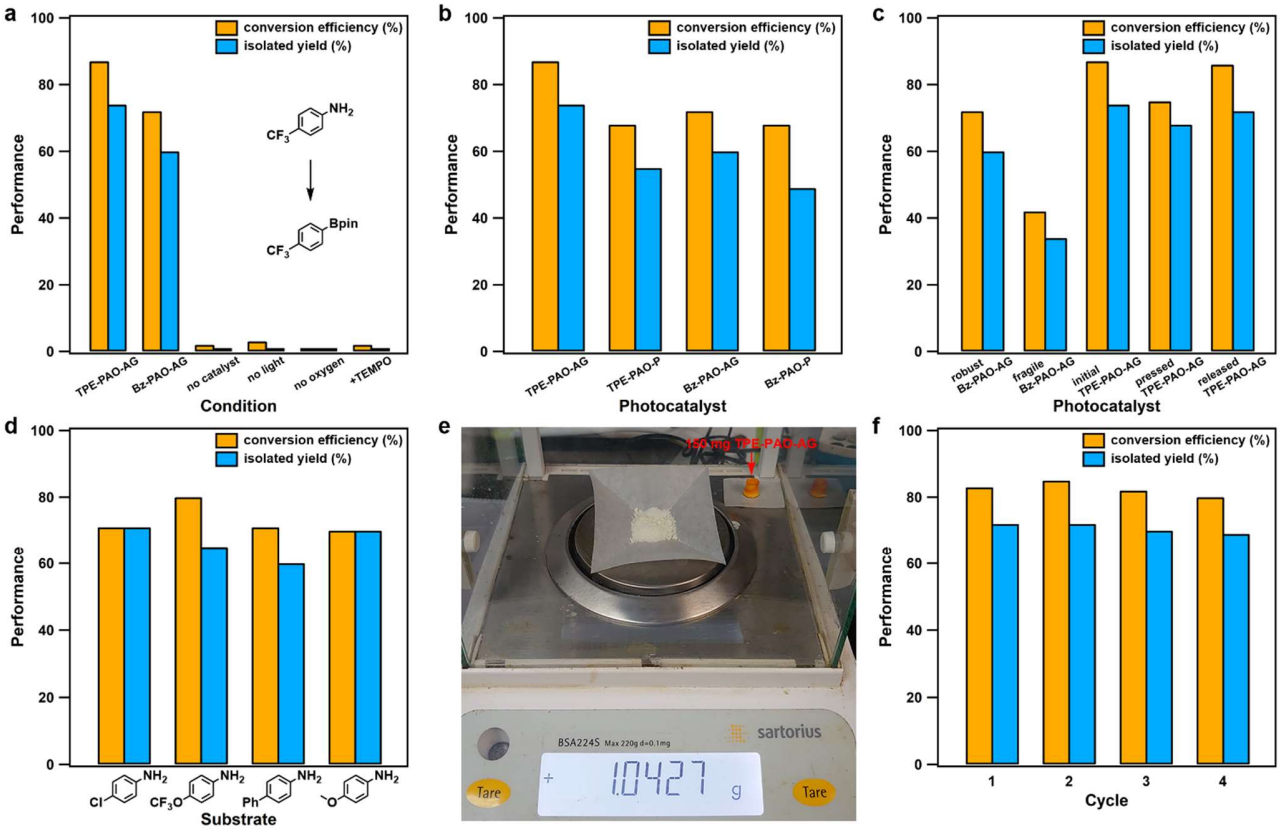

Figure 3. Performances of deaminative borylation using CMP aerogel-based quasi-homogeneous photocatalysts. (a) The conversion efficiencies and isolated yields of deaminative borylation using CMP aerogel-based quasi-homogeneous photocatalysts under optimized and controlled conditions. (b) The conversion efficiencies and isolated yields of deaminative borylation using CMP aerogels and powders as photocatalysts. (c) The conversion efficiencies and isolated yields of deaminative borylation using robust and fragile CMP aerogels as photocatalysts, and using CMP aerogels under initial, pressed, and released conditions. (d) The conversion efficiencies and isolated yields of deaminative borylation for different amino substrates. (e) Photo of 1.04 g 4,4,5,5-tetramethyl-2-(4-(trifluoromethyl)phenyl)-1,3,2-dioxaborolane product synthesized by the photocatalysis of 150 mg **TPE-PAO-AG**. (f) Cycling tests of the photocatalysis by **TPE-PAO-AG**.

We further exploited the CMP aerogels as reactors for quasi-homogeneous photocatalysis of direct deaminative borylation. Different from the traditional Grignard or aryllithium reagents approaches that require rigorous anhydrous conditions and with narrow functional-group compatibility,[33] borylation from arylamines is more attractive because arylamines are abundant and cheap raw materials that allow the borylation reaction to occur solely on the amino groups with good site selectivity. However, because of the high dissociation energy of the C–N bond, the current borylation from arylamines usually involves reactive intermediates such as diazonium salts and aryl ammonium salts.[23,34] Direct transformations of primary amines bypassing intermediates thus remain challenging, though few works have been reported using small-molecular photocatalysts.[33–35]

The CMP aerogels-based quasi-homogeneous photocatalysis was readily performed at room temperature by absorbing the reaction solutions into a patch of thin aerogel to form a semitransparent wet gel, in which high-concentration catalytic reaction centers fully surround the reactants. After the reaction, the products were washed out of the gels to generate recycled aerogels for continuous reactions. We first selected the borylation of 4-(trifluoromethyl)aniline as a model reaction. After optimizing the reaction conditions (Tables S1–S5), a typical experiment was performed using **TPE-PAO-AG** (#2) or **Bz-PAO-AG** (#2) to catalyze 4-(trifluoromethyl)aniline in a 4,4,4',4',5,5,5',5'-octamethyl-2,2'-bi(1,3,2-dioxaborolane) (B_2pin_2)-containing dioxane solution in the presence of white light and O_2 at room temperature for 15 h. **TPE-PAO-AG** exhibited conversion efficiency and isolated yield of 87% and 74%, respectively (Figure 3a, Table S6, entry 1, Figure S54), higher than the **Bz-PAO-AG** photocatalyst (72% and 60%, respectively, Figure 3a, Table S6, entry 2). This conversion efficiency is the highest reported for the deaminative borylation from primary anilines.[33–35] Moreover, our CMP aerogel photocatalysts only require O_2, without any need for auxiliary oxidants and metal catalysts. The solid-state nature of the CMP aerogels allows for the facile separation of products, compared to homogeneous catalysis, which requires tedious separation. The reactions were prohibited in the absence of photocatalyst, light, or O_2 (Figure 3a, Table S6, entries 3–5). Additionally, when 2,2,6,6-tetramethylpiperidinyl-1-oxide (TEMPO) was added as a radical inhibitor, almost no product was observed (Figure 3a, Table S6, entry 7). This suggests that, after absorbing light to generate electron-hole pairs, the key mechanistic steps involve sensitization of triplet oxygen to singlet oxygen and oxidation of the substrates to the products (Figure S55, S56).

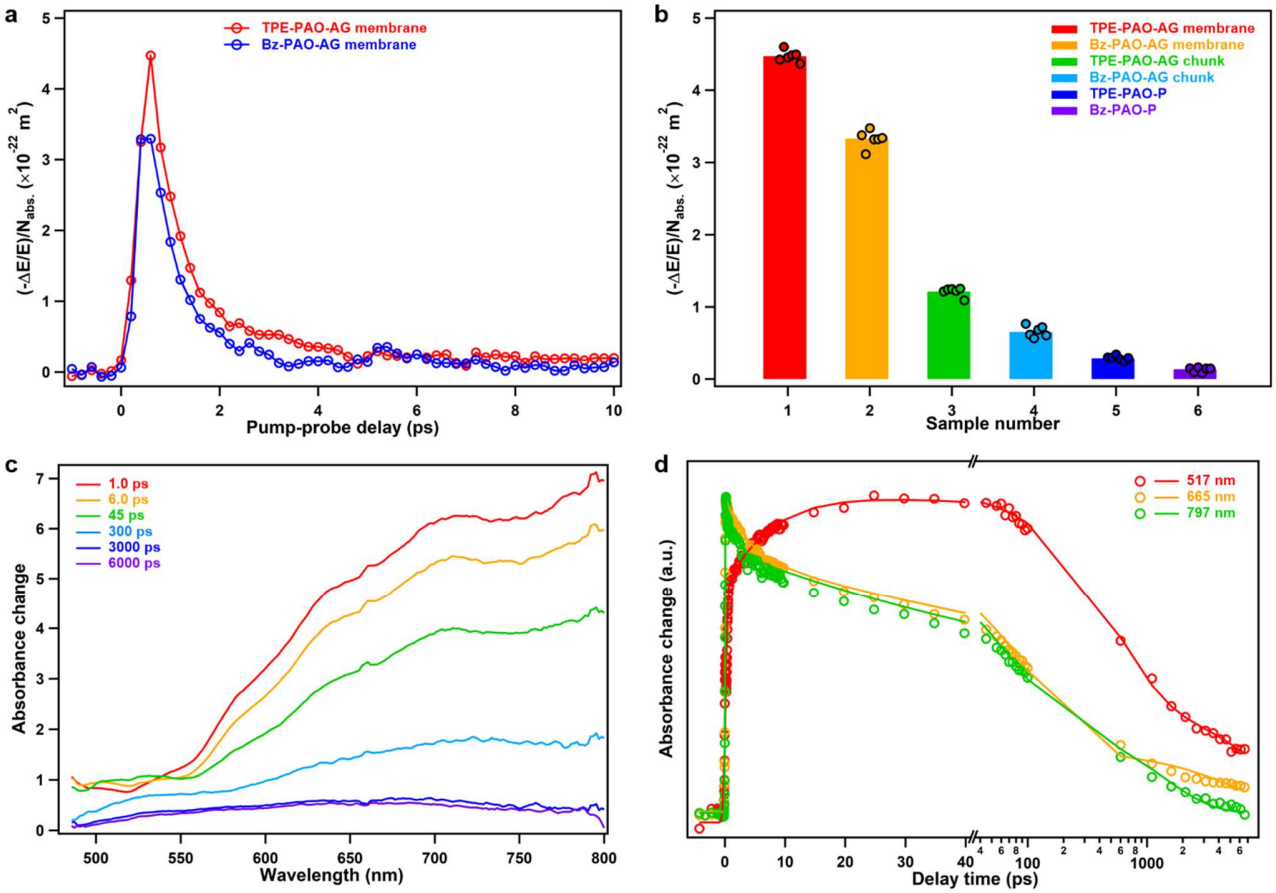

Figure 4. Charge-carrier dynamics of TPE-PAO-AG and Bz-PAO-AG. (a) THz photoconductivity dynamics of **TPE-PAO-AG** and **Bz-PAO-AG** membranes. The samples were photoexcited by an ultrashort laser pulse of 3.1 eV in a dry N_2-purged atmosphere. (b) Comparison of the charge-transport properties among different materials and forms. Circles represent the value of each sample point, while bars represent the average of the six sample points on each sample. (c) Time-resolved absorption spectra at an indicated time delay for **TPE-PAO-AG** membrane. (d) Normalized kinetic curves of **TPE-PAO-AG** membrane at representative wavelengths, showing the correlation between 517-, 665-, and 797-nm traces.

We found that the macroscopic forms and the mechanical properties played an important role in the catalytic performance. The CMP powders showed substantially lower conversion efficiencies and isolated yields compared to their corresponding aerogel photocatalysts (Figure 3b, Table S7), revealing that the CMP powder dispersed in the reaction solutions was inefficient for such a challenging reaction because of insufficient catalytic reaction centers in the diluted CMP dispersing solutions. This comparison demonstrated the advantage of quasi-homogeneous photocatalysis to heterogeneous photocatalysis. Another control experiment was to synthesize fragile CMP gels using a substantially lower DAPAO concentration of 0.025 M. In this case, **TPE-PAO-G** failed to form, whereas **Bz-PAO-G** and **Bz-PAO-AG** were easily cracked when touched with tweezers. Photocatalysis using the fragile **Bz-PAO-AG** afforded the conversion efficiency and isolated yield of 42% and 34%, respectively (Figure 3c, Table S8), substantially lower than **Bz-PAO-AG** (#2) (72% and 60%, respectively, Figure 3c). Moreover, fragile **Bz-PAO-AG** was difficult to recycle as it was damaged during solvent washing and refreshing. These results revealed the importance of macroscopic mechanical strength on the photocatalytic performance of the CMP aerogels. A more powerful necessity statement for using such ultrastiff CMP aerogels for quasi-homogeneous photocatalysis was further demonstrated by compressing **TPE-PAO-G** by ~30 vol.% using two quartz plates. In this case, **TPE-PAO-G** successfully catalyzed the reaction with retained conversion efficiency and isolated yield of 75% and 68%, respectively (Figure 3c, Table S9), remaining undamaged at the macroscopic scale with recovered conversion efficiency (86%) and isolated yield (72%) after the pressure was released. This result demonstrated that the ultrastiff CMP aerogels exhibit pressure tolerance, which is promising for real catalytic systems.

We further evaluated the generality of **TPE-PAO-AG** as a photocatalyst. Several primary anilines with either electron-donating or electron-withdrawing substituents were employed as substrates. **TPE-PAO-AG** could convert all of them into the desired products in high yields (Figure 3d, Table S10, Figures S57–S60). Furthermore, **TPE-PAO-AG** was employed for scale-up synthesis using larger aerogels. A chunk of 150 mg **TPE-PAO-AG** successfully catalyzed the deaminative borylation reaction, with one batch production of over 1 g in an isolated yield of 76% (Figure 3e). This result demonstrated the potential of CMP aerogel-based quasi-homogeneous photocatalysis for scale-up synthesis in view of potential industrial applications. The recycling test showed that **TPE-PAO-AG** was stable under four consecutive cycles, and the conversion efficiency and isolated yield remained around 80% and 70%, respectively

(Figure 3f). After recycling, the mechanical properties of **TPE-PAO-AG** remained almost unchanged (Figure S61), which was presumably because of undamaged macrostructures (Figure S62).

Charge-carrier dynamics.

To uncover the exceptional photocatalytic activity from the photophysical aspects, we combined time-resolved terahertz spectroscopy (TRTS, see Supplementary Materials)[36] and transient absorption (TA) spectroscopy[23]. While TRTS mainly reports free carrier dynamics, TA can provide information on both free carriers and bound electron-hole pairs (i.e., excitons).

First, to assess the photoconductivity of the samples and elucidate the role of morphology in determining charge-transport properties, we measured the CMP samples in the forms of aerogel membranes, bulky aerogels, and stirring-synthesized powders by TRTS. In the TRTS measurements, we optically injected charge carriers into the samples by a 3.1-eV ultrashort laser pulse, and the pump-induced conductivity evolution was examined by a single-cycle THz pulse with a field strength of E. The pump-induced relative THz peak field attenuation ($-\Delta E/E$) scales linearly with photoconductivity ($\sigma = e \cdot N_{abs} \cdot \varphi \cdot \mu$, with N_{abs}, φ, μ representing absorbed photon density, free-carrier generation quantum yield, and carrier mobility. Here, we compare the $-\Delta E/E$ divided by N_{abs} of varied samples to provide a direct comparison of the product of carrier mobility and free carrier generation quantum yield $\varphi \cdot \mu$. Taking the **TPE-PAO-AG** and **Bz-PAO-AG** membranes as examples, the photoexcitation triggered a sub-ps rise in conductivity due to the photogenerated free charge carriers (Figure 4a). Subsequently, the transient photoconductivity decays to null on a ps timescale, resulting from free carrier trapping (e.g., at the catalytic centers) and/or the formation of bound excitons. The free carrier nature is evidenced by the nearly zero imaginary conductivity on all time scales (up to ns, Figure S63). The $\varphi \cdot \mu$ values of **TPE-PAO-AG** and **Bz-PAO-AG** membranes were estimated to be $(2.2 \pm 0.1) \times 10^{-3}$ and $(1.6 \pm 0.1) \times 10^{-3}$ cm^2 V^{-1} s^{-1}, respectively. Since $0 \leq \varphi \leq 100\%$ (see details in Supporting Information), the estimated values represent the lower bounds of μ. These values are sufficiently high for amorphous organic/polymer semiconductors to achieve efficient photocatalysis. We further compared the charge-transport properties of the CMP samples with different macroscopic forms (Figure S64). **TPE-PAO-AG** consistently showed much-enhanced photoresponse compared to **Bz-PAO-AG**, whereas the photoresponse of the aerogel membranes was approximately 20 times higher than that of the stirring-synthesized powders (Figure 4b), highlighting the importance of macroscopic porous materials with percolated CMP networks for efficient charge-carrier migration.

The femtosecond TA technique was carried out on the **TPE-PAO-AG** membrane to investigate the excited-state dynamics. The excited state absorption (ESA) system consists of a broad absorption covering 500-750 nm (Figure 4c), with several underlying features. The long-wavelength response exhibits indistinguishable dynamics, as apparent from the 665- and 797-nm traces (Figure 4d). An obvious anti-correlation between the 665-/797-nm decay and the 517-nm rise was observed (Figure 4d). Global analysis of the 517- and 797-nm kinetic curves resulted in a rapid time constant of 7.8 ps. This rise time in TA studies (sensitive to excitons) was roughly on the same time scale as the THz photoconductivity decay (sensitive to free carriers). This indicates that part, if not all, of the photogenerated free carriers, were converted into excitons. The component at ~800 nm was simultaneously generated upon excitation and could be assigned to S_1, whereas the new-emerging component at ~520 nm was efficiently produced at the expense of S_1. Moreover, its spectral feature showed no appreciable temporal evolution beyond the ns time scale (blue and purple lines in Figure 4c). Given its long-lived nature, we tentatively attribute this component to the T_1 state generated via intersystem crossing or singlet fission[23], providing sufficient time for efficient charge-carrier extraction. Combined spectroscopic studies indicated the presence of relatively high-mobility, short-lived free carriers, and long-lived excitonic species in the system, which underlies the photocatalytic performance.

Conclusion.

In summary, this work demonstrates efficient quasi-homogeneous photocatalysis by constructing ultrastiff CMP aerogels with exceptional charge-transport properties. The cooperation of hierarchical porosity, macroscopic stiffness, and microscopic photoactivity allows the use of CMP aerogels as reactors for quasi-homogeneous photocatalysis of direct deaminative borylation with record-high efficiency and gram-scale productivity. This synthetic rationale for macroscopic porous materials is more broadly suitable for use with diverse porous polymers for designing efficient quasi-homogeneous catalysts as well as broadening their advanced applications.

ASSOCIATED CONTENT

Supporting Information.
Synthetic procedures, FT-IR, SEM, PXRD, TG, gas adsorption, DMA test, TR-DLS, UV-vis spectra, and ^{1}H NMR. This material is available free of charge via the Internet at http://pubs.acs.org.

AUTHOR INFORMATION

Corresponding Author

*gucheng@scu.edu.cn,
shuhei.furukawa@icems.kyoto-u.ac.jp,
huanglb@scut.edu.cn

Author Contributions

#These authors contributed equally.

Notes

The authors declare no competing financial interest.

ACKNOWLEDGMENT

This work was supported by the National Natural Science Foundation of China (grant nos. 21975078, 21971074), the Fundamental Research Funds for the Central Universities, the start-up foundation of Sichuan University, and the KAKENHI Grant-in-Aid for Scientific Research (S) (grant nos. JP18H05262, JP22H05005) from the Japan Society of the Promotion of Science (JSPS). We thank Dr. Jiaming Chen (MPIP) for additional THz measurements, Mr. Xianzhe Wei for additional porosity measurements, and the iCeMS analysis center for access to the analytical instruments.

REFERENCES

(1) Hoffmann, M. R.; Martin, S. T.; Choi, W.; Bahnemann, D. W. Environmental Applications of Semiconductor Photocatalysis. *Chem. Rev.* **1995**, *95*, 69–96.

(2) Tong, H.; Ouyang, S.; Bi, Y.; Umezawa, N.; Oshikiri, M.; Ye, J. Nano-Photocatalytic Materials: Possibilities and Challenges. *Adv. Mater.* **2012**, *24*, 229–251.

(3) Wan, W.; Zhang, R.; Ma, M.; Zhou, Y. Monolithic Aerogel Photocatalysts: A Review. *J. Mater. Chem. A* **2018**, *6*, 754–775.

(4) Prier, C. K.; Rankic, D. A.; MacMillan, D. W. C. Visible Light Photoredox Catalysis with Transition Metal Complexes: Applications in Organic Synthesis. *Chem. Rev.* **2013**, *113*, 5322–5363.

(5) Genzink, M. J.; Kidd, J. B.; Swords, W. B.; Yoon, T. P. Chiral Photocatalyst Structures in Asymmetric Photochemical Synthesis. *Chem. Rev.* **2022**, *122*, 1654–1716.

(6) Banerjee, T.; Podjaski, F.; Kröger, J.; Biswal, B. P.; Lotsch, B. V. Polymer Photocatalysts for Solar-to-Chemical Energy Conversion. *Nat. Rev. Mater.* **2021**, *6*, 168–190.

(7) Lee, J.-S. M.; Cooper, A. I. Advances in Conjugated Microporous Polymers. *Chem. Rev.* **2020**, *120*, 2171–2214.

(8) Luo, S.; Zeng, Z.; Zeng, G.; Liu, Z.; Xiao, R.; Xu, P.; Wang, H.; Huang, D.; Liu, Y.; Shao, B.; Liang, Q.; Wang, D.; He, Q.; Qin, L.; Fu, Y. Recent Advances in Conjugated Microporous Polymers for Photocatalysis: Designs, Applications, and Prospects. *J. Mater. Chem. A* **2020**, *8*, 6434–6470.

(9) Zhao, C.; Chen, Z.; Shi, R.; Yang, X.; Zhang, T. Recent Advances in Conjugated Polymers for Visible-Light-Driven Water Splitting. *Adv. Mater.* **2020**, *32*, 1907296.

(10) Zhang, Z.; Jia, J.; Zhi, Y.; Ma, S.; Liu, X. Porous Organic Polymers for Light-Driven Organic Transformations. *Chem. Soc. Rev.* **2022**, *51*, 2444–2490.

(11) Dadashi-Silab, S.; Lorandi, F.; DiTucci, M. J.; Sun, M.; Szczepaniak, G.; Liu, T.; Matyjaszewski, K. Conjugated Cross-Linked Phenothiazines as Green or Red Light Heterogeneous Photocatalysts for Copper-Catalyzed Atom Transfer Radical Polymerization. *J. Am. Chem. Soc.* **2021**, *143*, 9630–9638.

(12) Wang, H.; Jin, S.; Zhang, X.; Xie, Y. Excitonic Effects in Polymeric Photocatalysts. *Angew. Chem. Int. Ed.* **2020**, *59*, 22828–22839.

(13) Li, G.; Fu, P.; Yue, Q.; Ma, F.; Zhao, X.; Dong, S.; Han, X.; Zhou, Y.; Wang, J. Boosting Exciton Dissociation by Regulating Dielectric Constant in Covalent Organic Framework for Photocatalysis. *Chem Catal.* **2022**, *2*, 1734–1747.

(14) Das, S.; Ben, T.; Qiu, S. Shaping of Porous Polymers. *Polymer* **2020**, *207*, 122928.

(15) Wang, L.; Su, Y.; Gu, C. Solution Processing of Cross-Linked Porous Organic Polymers. *Acc. Mater. Res.* **2022**, *3*, 1049–1060.

(16) Koner, K.; Sadhukhan, A.; Karak, S.; Sasmal, H. S.; Ogaeri, Y.; Nishiyama, Y.; Zhao, S.; Položij, M.; Kuc, A.; Heine, T.; Banerjee, R. Bottom-Up Synthesis of Crystalline Covalent Organic Framework Nanosheets, Nanotubes, and Kippah Vesicles: An Odd–Even Effect Induction. *J. Am. Chem. Soc.* **2023**, *145*, 14475–14483.

(17) Mohammed, A. K.; Usgaonkar, S.; Kanheerampockil, F.; Karak, S.; Halder, A.; Tharkar, M.; Addicoat, M.; Ajithkumar, T. G.; Banerjee, R. Connecting Microscopic Structures, Mesoscale Assemblies, and Macroscopic Architectures in 3D-Printed Hierarchical Porous Covalent Organic Framework Foams. *J. Am. Chem. Soc.* **2020**, *142*, 8252–8261.

(18) Du, R.; Zhang, N.; Xu, H.; Mao, N.; Duan, W.; Wang, J.; Zhao, Q.; Liu, Z.; Zhang, J. CMP Aerogels: Ultrahigh-Surface-Area Carbon-Based Monolithic Materials with Superb Sorption Performance. *Adv. Mater.* **2014**, *26*, 8053–8058.

(19) Zhu, D.; Zhu, Y.; Yan, Q.; Barnes, M.; Liu, F.; Yu, P.; Tseng, C.-P.; Tjahjono, N.; Huang, P.-C.; Rahman, M. M.; Egap, E.; Ajayan, P. M.; Verduzco, R. Pure Crystalline Covalent Organic Framework Aerogels. *Chem. Mater.* **2021**, *33*, 4216–4224.

(20) Martín-Illán, J. Á.; Rodríguez-San-Miguel, D.; Castillo, O.; Beobide, G.; Perez-Carvajal, J.; Imaz, I.; Maspoch, D.; Zamora, F. Macroscopic Ultralight Aerogel Monoliths of Imine-Based Covalent Organic Frameworks. *Angew. Chem. Int. Ed.* **2021**, *60*, 13969–13977.

(21) Li, A.; Cao, Q.; Zhou, G.; Schmidt, B. V. K. J.; Zhu, W.; Yuan, X.; Huo, H.; Gong, J.; Antonietti, M. Three-Phase Photocatalysis for the Enhanced Selectivity and Activity of CO_2 Reduction on a Hydrophobic Surface. *Angew. Chem. Int. Ed.* **2019**, *58*, 14549–14555.

(22) Huo, H.; He, H.; Huang, C.; Guan, X.; Wu, F.; Du, Y.; Xing, H.; Kan, E.; Li, A. Solar-Driven CO_2-to-Ethanol Conversion Enabled by Continuous CO_2 Transport via a Superhydrophobic Cu_2O Nano Fence. *Chem. Sci.* **2024**, *15*, 1638–1647.

(23) Wang, L.; Liu, X.; Shi, X.; Anderson, C. L.; Klivansky, L. M.; Liu, Y.; Wu, Y.; Chen, J.; Yao, J.; Fu, H. Singlet Fission in a Para-Azaquinodimethane-based Quinoidal Conjugated Polymer. *J. Am. Chem. Soc.* **2020**, *142*, 17892–17896.

(24) Mo, F.; Jiang, Y.; Qiu, D.; Zhang, Y.; Wang, J. Direct Conversion of Arylamines to Pinacol Boronates: A Metal-Free Borylation Process. *Angew. Chem. Int. Ed.* **2010**, *49*, 1846–1849.

(25) Zheng, X.; Lee, H.; Weisgraber, T. H.; Shusteff, M.; DeOtte, J.; Duoss, E. B.; Kuntz, J. D.; Biener, M. M.; Ge, Q.; Jackson, J. A.; Kucheyev, S. O.; Fang, N. X.; Spadaccini, C. M. Ultralight, Ultrastiff Mechanical Metamaterials. *Science* **2014**, *344*, 1373–1377.

(26) Worsley, M. A.; Kucheyev, S. O.; Satcher, J. H.; Jr. Hamza, A. V.; Baumann, T. F. Mechanically Robust and Electrically Conductive Carbon Nanotube Foams. *Appl. Phys. Lett.* **2009**, *94*, 073115.

(27) Vallejo-Sánchez, D.; Amo-Ochoa, P.; Beobide, G.; Castillo, O.; Fröba, M.; Hoffmann, F.; Luque, A.; Ocón, P.; Pérez-Yáñez, S. Chemically Resistant, Shapeable, and Conducting Metal-Organic Gels and Aerogels Built from Dithiooxamidato Ligand. *Adv. Funct. Mater.* **2017**, *27*, 1605448.

(28) Rostami, J.; Benselfelt, T.; Maddalena, L.; Avci, C.; Sellman, F. A.; Ciftci, G. C.; Larsson, P. A.; Carosio, F.; Akhtar, F.; Tian, W.; Wågberg, L. Shaping 90 wt% Nanomofs into Robust Multifunctional Aerogels Using Tailored Bio-based Nanofibrils. *Adv. Mater.* **2022**, *34*, 2204800.

(29) Wang, C.; Eisenreich, F.; Tomović, Ž. Closed-Loop Recyclable High-Performance Polyimine Aerogels Derived from Bio-based Resources. *Adv. Mater.* **2023**, *35*, 2209003.

(30) Hu, P.; Wang, J.; Zhang, P.; Wu, F.; Cheng, Y.; Wang, J.; Sun, Z. M. Hyperelastic Kevlar Nanofiber Aerogels as Robust Thermal Switches for Smart Thermal Management. *Adv. Mater.* **2023**, *35*, 2207638.

(31) Su, Y.; Wang, Z.; Legrand, A.; Aoyama, T.; Ma, N.; Wang, W.; Otake, K.-i.; Urayama, K.; Horike, S.; Kitagawa, S.; Furukawa, S.; Gu, C. Hypercrosslinked Polymer Gels as a Synthetic Hybridization Platform for Designing Versatile Molecular Separators. *J. Am. Chem. Soc.* **2022**, *144*, 6861–6870.

(32) Tanimu, A.; Jaenicke, S.; Alhooshani, K. Heterogeneous Catalysis in Continuous Flow Microreactors: A Review of Methods and Applications. *Chem. Eng. J.* **2017**, *327*, 792–821.

(33) Shiozuka, A.; Sekine, K.; Toki, T.; Kawashima, K.; Mori, T.; Kuninobu, Y. Photoinduced Divergent Deaminative Borylation and Hydrodeamination of Primary Aromatic Amines. *Org. Lett.* **2022**, *24*, 4281–4285.

(34) Ahammed, S.; Nandi, S.; Kundu, D.; Ranu, B. C. One-Pot Suzuki Coupling of Aromatic Amines via Visible Light Photocatalyzed Metal Free Borylation Using *T*-Buono at Room Temperature. *Tetrahedron Lett.* **2016**, *57*, 1551–1554.

(35) Ji, S.; Qin, S.; Yin, C.; Luo, L.; Zhang, H. Unreactive C–N Bond Activation of Anilines via Photoinduced Aerobic Borylation. *Org. Lett.* **2022**, *24*, 64–68.

(36) Ulbricht, R.; Hendry, E.; Shan, J.; Heinz, T. F.; Bonn, M. Carrier Dynamics in Semiconductors Studied with Time-Resolved Terahertz Spectroscopy. *Rev. Mod. Phys.* **2011**, *83*, 543–586.

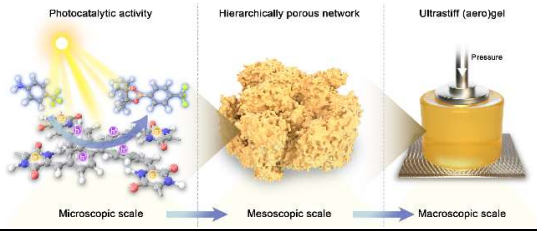
Photocatalytic activity
Hierarchically porous network
Ultrastiff (aero)gel
Pressure
Microscopic scale
Mesoscopic scale
Macroscopic scale